Seamless High-math xmlns="http://www.w3.org/1998/Math/MathML" display="inline">mi>Q/mi>/math> Microwave Cavities for Multimode Circuit Quantum Electrodynamics

Srivatsan Chakram, Andrew E. Oriani, Ravi K. Naik, Akash V. Dixit, Kevin He, Ankur Agrawal, Hyeokshin Kwon, and David I. Schuster

Seamless high-Q microwave cavities for multimode circuit QED

Srivatsan Chakram,[1, 2, 3, *] Andrew E. Oriani,[1, 4, *] Ravi K. Naik,[1, 2, 5] Akash V. Dixit,[1, 2]
Kevin He,[1, 2] Ankur Agrawal,[1, 2] Hyeokshin Kwon,[6] and David I. Schuster[1, 2, 4, †]

[1] *James Franck Institute, University of Chicago, Chicago, Illinois 60637, USA*
[2] *Department of Physics, University of Chicago, Chicago, Illinois 60637, USA*
[3] *Department of Physics and Astronomy, Rutgers University, Piscataway, New Jersey 08854, USA*
[4] *Pritzker School of Molecular Engineering, University of Chicago, Chicago, Illinois 60637, USA*
[5] *Department of Physics, University of California Berkeley, California 94720, USA*
[6] *Samsung Advanced Institute of Technology (SAIT),*
Samsung Electronics Co., Ltd, Suwon, Republic of Korea

Multimode cavity quantum electrodynamics —where a two-level system interacts simultaneously with many cavity modes—provides a versatile framework for quantum information processing and quantum optics. Due to the combination of long coherence times and large interaction strengths, one of the leading experimental platforms for cavity QED involves coupling a superconducting circuit to a 3D microwave cavity. In this work, we realize a 3D multimode circuit QED system with single photon lifetimes of 2 ms across 9 modes of a novel seamless cavity. We demonstrate a variety of protocols for universal single-mode quantum control applicable across all cavity modes, using only a single drive line. We achieve this by developing a straightforward *flute* method for creating monolithic superconducting microwave cavities that reduces loss while simultaneously allowing control of the mode spectrum and mode-qubit interaction. We highlight the flexibility and ease of implementation of this technique by using it to fabricate a variety of 3D cavity geometries, providing a template for engineering multimode quantum systems with exceptionally low dissipation. This work is an important step towards realizing hardware efficient random access quantum memories and processors, and for exploring quantum many-body physics with photons.

Circuit quantum electrodynamics (cQED) [1] has emerged as the preeminent platform for quantum optics and realizing quantum memories [2]. While studies of quantum optics with cQED have largely been restricted to a single or few cavity modes, the extension of cQED to many cavity modes (multimode cQED) promises explorations of many-body physics with exquisite single photon control. Multimode cavities are an efficient way of realizing many co-located cavity modes that can be simultaneously coupled to and controlled by a single physical qubit, ideal for creating multi-qubit quantum memories while reducing the number of physical lines required. A challenge currently limiting applications of multimode cQED in quantum information science—and the scaling to larger systems—is the need for longer coherence times.

3D superconducting cavities possess the longest coherence times in cQED [3], and while being intrinsically linear, can be strongly coupled to a nonlinear superconducting transmon circuit to realize universal gate operations [4, 5]. The resulting high cooperativities have enabled many fundamental experiments in quantum information science and quantum optics, including demonstrations of quantum error correction [6–8] and fault tolerance [9]. While quantum control has also been extended to two-cavity modes coupled to the same qubit [10], where it has been used to mediate gate operations and interactions [11, 12], it has so far not been extended to many cavity modes. Building multimode systems that leverage 3D cavities will enable explorations of a new regime of many-body quantum optics. Using a single physical qubit to control a multimode memory also allows us to potentially multiplex $\sim 10 - 1000$ modes, thereby providing a promising solution to the problem of wiring large quantum processors, and allowing superconducting quantum systems to go beyond the noisy intermediate-scale quantum era [13, 14].

Multimode cQED systems with strong light-matter interactions have been realized in a variety of 2D quantum circuits, with a Josephson-junction-based superconducting qubit coupled to many nearly harmonic modes. These include transmission line resonators [15], superconducting lumped-element [16–18] and Josephson-junction-based meta-materials [19], and electromechanical systems [20], highlighting the breadth of quantum optics and simulation problems that can be addressed with multimode cQED [21]. A multimode cQED system comprising a chain of strongly coupled coplanar waveguide resonators was also used to realize a random access quantum processor in which a single transmon mediated gate operations between arbitrary mode pairs [22]. For scaling such multiplexed systems to larger Hilbert spaces, the harmonic modes (quantum memories) must have much longer coherence times than the transmon qubit (quantum bus).

In this letter, we demonstrate a flexible 3D multimode cavity platform capable of high cooperativities across many cavity modes. To do this, we develop a new *flute* technique that enables the creation of a variety of cavity geometries while eliminating seam loss—arising from supercurrents crossing mechanical interfaces—present in the construction of many cavity designs. Using this technique, we realize a state-of-the-art multimode cQED sys-
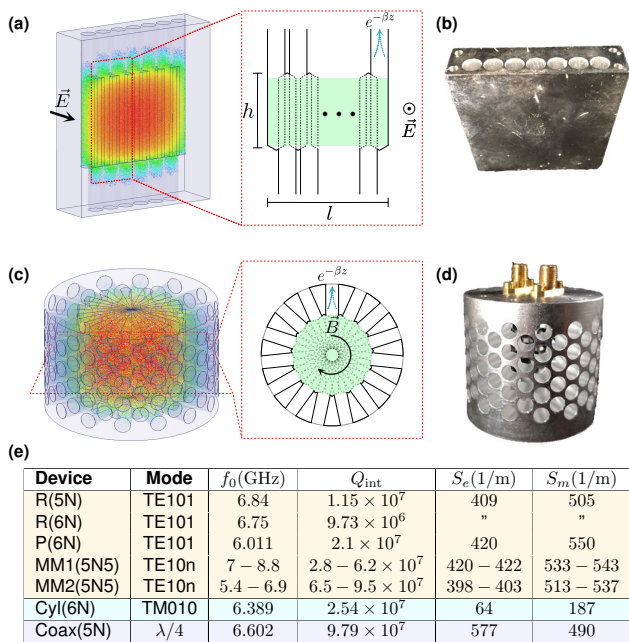
FIG. 1. **Outline of seamless _flute_ cavity design**. (a) An FE model showing the $\vec{E}$-field magnitude for the TE_{101} mode of a rectangular waveguide cavity. (inset) A side-view cutaway of the flute design highlighting the overlapping holes, with the effective mode volume highlighted in green. The evanescent decay through the holes is also shown, where β is the waveguide propagation constant for the TM_{0m} modes of the hole. (b) A picture of the R(5N) cavity. (c) An FE model of a cylindrical style flute cavity showing the $\vec{E}$-field magnitude for the fundamental TM_{010} mode. (inset) A top-view cutaway showing the effective mode volume created by the hole overlap. (d) A picture of the C(6N) cavity. (e) A table outlining the performance of various cavity geometries, highlighting the internal quality factors (Q_{int}), and the magnetic (S_m) and electric (S_e) participation ratios from FE simulations.

tem consisting of a monolithic 3D multimode cavity with coherence times exceeding 2 ms across the mode spectrum. We perform quantum operations on 9 of the cavity modes using a single superconducting transmon circuit placed at one end of the cavity, extending a variety of universal cavity control schemes—based on the dispersive interaction—to a multimode system.

The flute technique creates a cavity through the overlap of holes drilled from the top and bottom of a monolithic piece of superconductor, resulting in the generation of a cavity volume with no seams. This is illustrated in Fig. 1 (a) and (c) for a rectangular and cylindrical cavity, where we show finite element (FE) simulations of the fundamental cavity mode and visualize the creation of the cavity volume through the overlap of the holes (insets, cavity volume highlighted in green). The hole diameter is chosen such that the cutoff frequency of the waveguide mode is much higher than that of the cavity modes. This

ensures that the cavity mode energy density at the vacuum interface is exponentially suppressed, with the hole depth and diameter chosen such that the quality factor limit due to evanescent coupling to vacuum exceeds 10^9 for all the manipulable cavity modes (see Supplemental Material (SM) [23]), similar to the values for evanescent loss for a single mode coaxial $\lambda/4$ cavity [24]. As a result, despite the cavity being full of holes, we realize high quality factor cavities limited only by intrinsic losses.

We used the flute method to construct a number of cavities with various geometries, using aluminum ranging in purity from 5N (99.999%) to 6N (99.9999%), whose mode frequencies, quality factors, and geometric surface participation factors are summarized in the table in Fig 1 (e). In addition to the rectangular _pan-pipe_ [R(5N), R(6N), P(6N) [25]] and cylindrical cavities [Cyl(6N)] depicted in Fig. 1 (b) and (d) respectively, we also measured the coherence of rectangular multimode cavities [MM1(5N5), MM2(5N5)]. During fabrication, successive drilling and honing steps were used ensure a smooth and uniform finish of the cavity interior and to reduce the formation of metal burrs at the hole-cavity interface, followed by etching to remove surface damage induced from the manufacturing process. The average surface roughness after the full process was measured to be 2-3.6 μm for R5N (see SM [23]). We also measured the internal quality factor of a 5N aluminum coaxial $\lambda/4$ cavity that underwent the same etching process to be 97 million—comparable with the best quality factors observed in this cavity geometry in aluminum [26]. When the cavity losses are scaled by their geometric magnetic (S_m) and electric (S_e) surface participation ratios [3, 27], the MM2(5N5) cavity internal quality factors are comparable to those achieved in the coaxial cavity, ranging from $65-95$ million over the first 9 modes. The losses seen in the other cavity geometries differ by nearly a factor of 2 from that expected from the coaxial cavity Q even once the geometric scaling is taken into account, attributed to variations introduced in the manufacturing and surface treatment (See SM [23]).

While all 3D cavities are naturally multimodal, the usability of the modes depends on the mode frequencies, and the electric field participations at the qubit location. We achieve these requirements by using the TE_{10m} modes of a long rectangular waveguide cavity whose spectrum is given by $\nu_{1m} = \frac{c}{2}\sqrt{(1/h)^2 + (m/l)^2}$, where m is the mode number along the cavity length (l). The frequency of the fundamental mode (Fig. 2 (a)) is tuned by the cavity height (h), the second smallest cavity dimension. We operate on modes with a single antinode along h, and an increasing number of antinodes along l, as illustrated by the 9th mode in Fig. 2(b). In this regime, the mode spacing scales inversely with length, with the modes near the cutoff frequency having significant dispersion (dashed red lines in Fig 2(e)). We can change this dispersion by modulating the cavity height by varying the top and bottom hole overlap across the cavity length, with the quadratic

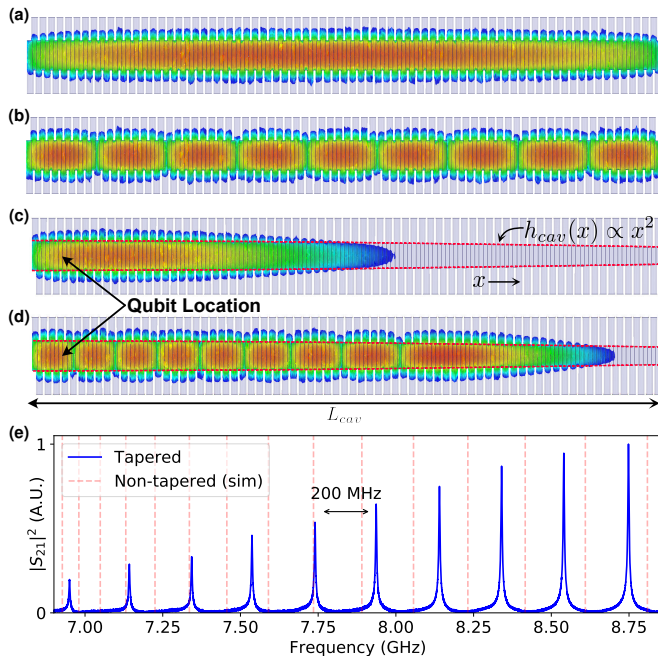| Device	Mode	f_0(GHz)	Q_{int}	S_e(1/m)	S_m(1/m)
R(5N)	TE_{101}	6.84	1.15×10^7	409	505
R(6N)	TE_{101}	6.75	9.73×10^6	"	"
P(6N)	TE_{101}	6.011	2.1×10^7	420	550
MM1(5N5)	TE_{10n}	$7-8.8$	$2.8-6.2 \times 10^7$	$420-422$	$533-543$
MM2(5N5)	TE_{10n}	$5.4-6.9$	$6.5-9.5 \times 10^7$	$398-403$	$513-537$
Cyl(6N)	TM_{010}	6.389	2.54×10^7	64	187
Coax(5N)	$\lambda/4$	6.602	9.79×10^7	577	490

FIG. 2. **Dispersion engineering in a multimode flute cavity** (a),(b) FE simulations showing the magnitude of the electric field ($|\vec{E}|$) for the first, and the ninth mode of a long rectangular cavity. (c),(d) $|\vec{E}|$ profile for a similar cavity with the height tapered according to the expression $h_{\text{cav}}(x) = h_0 - \alpha x^2$. (e) Mode spectrum of a tapered multimode flute cavity [MM1(5N5)] measured at room temperature (blue), and the simulated eigenfrequencies for a non-tapered cavity (red vertical lines) of the same length.

profile shown in Fig 2(c) and (d) resulting in a nearly constant mode spacing, demonstrated by the transmission measurement in Fig 2(e)(blue) for MM1(5N5). This has the additional effect of lensing the field towards one side of the cavity, increasing the coupling to the qubit (location indicated by arrows) for the higher order modes. We are therefore able to tune both the mode dispersion and mode-qubit coupling by modulating the cavity height. Increasing the cavity length leads to more modes in a given bandwidth, with the mode spacing being ultimately limited by off-resonant interactions between the qubit and non-target modes.

We control the cavity modes using a superconducting transmon circuit that serves as a quantum bus that couples to all the modes. The choice of the number of modes is also informed by the coherence times of the transmon and the cavity modes – the gate error while operating on a target mode should be comparable to the accumulated idle errors of the non-target modes. This suggests that the number of usable modes scales as $n_m = T_1^c/T_1^q$, where T_1^c and T_1^q are the cavity and qubit relaxation times respectively. With our average measured $T_1^c \sim 2$ ms and $T_1^q \sim 80 - 100 \ \mu s$, we are able to control Hilbert spaces

of ~ 10 modes before being limited by errors from multiplexing. The superconducting transmon circuit is simultaneously coupled to all the cavity modes by placing it at one end of the multimode flute cavity as shown in Fig. 3 (a), where the first 9 modes have couplings ranging from $50 - 170$ MHz. The capacitor pads of the transmon act as antennas that couple to the electric fields of the modes of the storage cavity (red) and a second adjacent smaller flute cavity used for readout (green). This interaction allows the cavity control operations developed in single-mode systems to be applied to any mode of the multimode cavity, all through a single drive line that couples directly to the readout resonator, corresponding to a ten-fold reduction in the number of control lines.

We demonstrate 3 different ways of controlling the cavity modes, all of which use the Josephson non-linearity of the transmon to exploit different physics of the system. These protocols differ in the required drive strengths, frequencies, and gates times, but result in similar infidelities up to prefactors in the regime where the transmon is the dominant source of decoherence. These are (1) resonant photon exchange mediated by 4-wave mixing processes, (2) cavity displacements used in conjunction with photon number selective phase gates (SNAP) [4], and (3) cavity drives within subspaces engineered by photon blockade [28, 29]. These schemes can also realize gate operations and interactions between modes. The control methods can all be understood by rewriting the junction phase in terms of the dressed states arising from the interaction with the modes, and expanding the transmon Josephson energy to quartic order:

$$H_I = \frac{\alpha}{12} \left(\beta_t \hat{c} + \sum_m \beta_m \hat{a}_m + \beta_r(\hat{a}_r + \xi_d) + \text{c.c} \right)^4 \quad (1)$$

Here, α is the transmon anharmonicity, and $\beta_t, \beta_r, \beta_m$ are the participations of the transmon, readout, and storage modes in the phase of the transmon junction, respectively. ξ_d is the combined readout and transmon drive displacement precessing at the drive frequency, and all operators are rotating at their natural frequencies (See SM [23]). This interaction leads to a 4-wave mixing process ($\sim \sqrt{\chi_m \chi_r} \hat{c}^2 \hat{a}_d^\dagger \xi_d/2$) that takes two photons in the transmon ($|f0_m\rangle$) to one photon in the storage mode ($|g1_m\rangle$) using a single-drive tone at their difference frequency, as illustrated in Fig. 3(b). This $|f0\rangle - |g1\rangle$ sideband ([11, 30]) can be used to perform SWAP operations on the modes in $0.5 - 1 \ \mu s$, and is illustrated in Fig. 3(c).

The interaction described in Eqn. 1 results in a dispersive shift ($\chi_m \hat{a}_m^\dagger \hat{a}_m \hat{c}^\dagger \hat{c}$) which leads to the qubit frequency being dependent on the photon number of each cavity, resulting in well-resolved transitions due to the high cooperativity [31]. In the SNAP protocol, we use a combination of number selective qubit rotations ($|gn_m\rangle \leftrightarrow |en_m\rangle$) and cavity displacements for universal control, as illustrated in Fig. 3(d). The pulse sequences
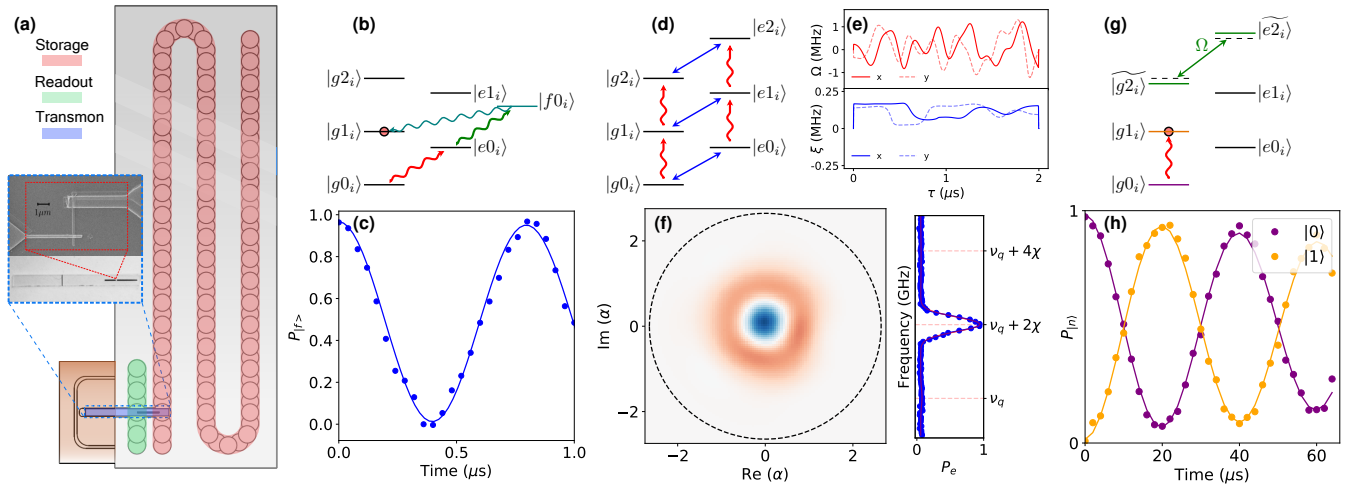
FIG. 3. **Quantum control of multimode flute cavity using a transmon**. (a) A schematic of the multimode flute cavity [MM2(5N5)] showing the location of the storage cavity (red), readout cavity (green), and transmon chip (blue). (b) Energy level diagram illustrating cavity state preparation using $|f0_i\rangle - |g1_i\rangle$ charge sideband transitions. (c) Corresponding sideband Rabi oscillations for mode 3 obtained after initializing the transmon in the $|f\rangle$ state, and driving at the $|f0_3\rangle - |g1_3\rangle$ difference frequency. (d) Energy level diagram illustrating control of the cavity using SNAP gates with resonant drives on the cavity (red) and the transmon (blue). (e) x (solid) and y (dashed) quadratures of the optimal control pulses acting on the transmon (Ω, top) and the cavity (ξ, bottom), used to prepare cavity mode 2 in $|1\rangle$. (f) Measurement of the resulting state using Wigner tomography (left), and photon number resolved qubit spectroscopy (right). (g) Energy level diagram illustrating state preparation by photon blockade using a resolved transmon pulse resonant with $|g2_i\rangle - |e2_i\rangle$ (green). The resulting Rabi splitting makes the cavity mode anharmonic, with a weak resonant cavity drive (red) producing Rabi oscillations, as shown in (h) for mode 3 (See SM [23]).

are obtained through optimal control using the gradient ascent pulse engineering (GrAPE) algorithm [5, 32]. The optimal control pulse shown in Fig. 3(e) is used to prepare Fock state $|1\rangle$ in mode 2, as shown in Fig. 3(f).

Resolved transmon drives resonant with transitions corresponding to different photon numbers can also be used to blockade selected states and thus carve the allowed Hilbert space that is connected by a single cavity drive tone. This is illustrated in Fig. 3(g), where a resonant $|g2_m\rangle - |e2_m\rangle$ drive hybridizes the states, selectively shifting their energies by the Rabi drive strength Ω (for $\Omega \ll \chi_m$). The cavity mode thus inherits an anharmonicity Ω, with the $|2\rangle$ state being blockaded [28]. A sufficiently weak cavity drive ($\epsilon \ll \Omega$) therefore results in a Rabi oscillation, as shown in Fig. 3(h), which can be used to prepare an arbitrary qubit state of $|0\rangle$, $|1\rangle$ in any cavity mode. This scheme can be generalized to perform universal operations on qudits realized in any mode, and to prepare multimode entangled states with appropriate choice of the blockade drive [29].

The fidelity of these cavity control protocols is limited primarily by decoherence arising from the transmon during the gate operation. The gate speed is set by the dispersive shift, shown as a function of the mode frequency for MM2(5N5) in Fig. 4(a, left). The minimum transmon-induced infidelty scales as $\sim 1/(\chi T_q)$ up to prefactors, where T_q is the minimum of the qubit decay and decoherence time. Although the transmon is only

directly occupied during the SNAP and resonant sideband SWAP gates, the minimum infidelity for photonblockade gates is also the same, after optimizing the drive strength to minimize leakage and blockade-induced Purcell decay. The gate fidelities are also a function of the instrinsic quality factors of the modes, which range from $65 - 95 \times 10^6$, as shown in Fig. 4(a, right). This results in an expected additional infidelity of 0.1 % for the sideband and SNAP gates, and $\sim 1 - 2$ % for the longer blockade gates (See SM [23]).

We characterize the decay and decoherence times of the cavity modes by T_1 and Ramsey measurements, the results of which are shown in Fig. 4(b). Here, each cavity mode is initialized in the $|1\rangle$ and $|0\rangle + |1\rangle$ states using cavity Rabi oscillations performed in the presence of photon blockade, as shown in Fig. 3(d). The T_1 times of all the cavity modes were ~ 2 ms, while the T_2 times range from $2 - 3$ ms (see SM [23]). The deviation of T_2 from $2T_1$ is consistent with additional dephasing from cavity frequency fluctuations arising from thermal excitations of the transmon (blue band in Fig. 4(b)). These coherence times are nearly two orders of magnitude better than those that have been reported in any multimode cQED system. The coherence times of any of these cavity modes is also comparable to the longest reported in single or few-mode 3D cQED systems.

In summary, we have demonstrated a new flute method for creating high quality factor seamless cavities with tai-
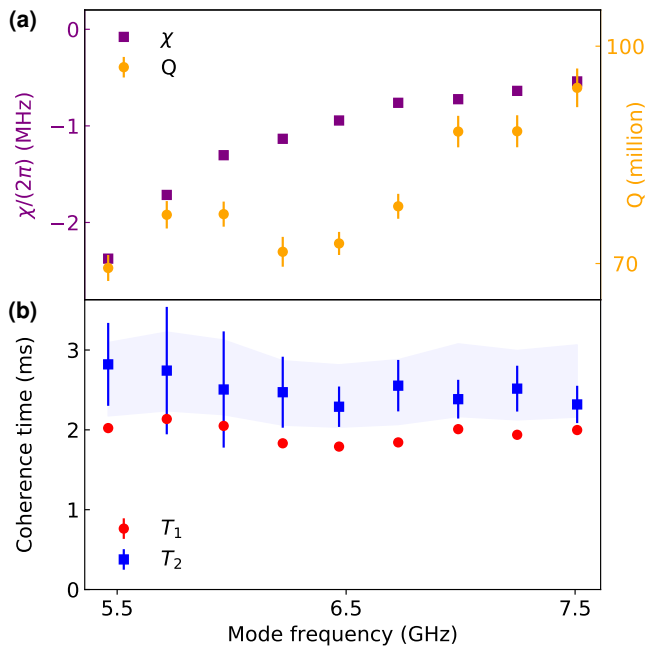
FIG. 4. **Dispersive shift and mode lifetimes**. (a) (left) Dispersive shift and (right) quality factors for the first 9 modes of the multimode storage cavity [MM2(5N5)]. (b) Cavity mode decoherence times (T_1, T_2) for the first 9 modes (See SM [23]). The blue region represents the theoretical mode T_2 limits arising from additional dephasing due to the thermal population of the transmon ($n_{th}^q = 1.2 \pm 0.5\%$).

lored mode-dispersion and mode-qubit couplings, ideally suited for creating multimode circuit-QED systems with high cooperativities across all modes. As quantum systems increase in volume and processor size, one of the most important challenges is the hardware overhead of lines and attendant equipment required for the control of every qubit or cavity mode. In this work we have demonstrated—with a single control line—a variety of schemes for universal control of ~10 cavity modes using the nonlinearity of a single transmon. This is an important step for realizing cavity-based random access memories and processors, and toward creating exotic many-body states of microwave photons, such as fractional quantum Hall phases [33, 34] and those stabilized by N-body interactions [29]. In principle, this control can be extended to ~1000 cavity modes by leveraging state-of-the-art niobium accelerator cavity technology to achieve single-photon lifetimes > 2s [35]. While we have demonstrated quantum control of a single multimode cavity, these systems can also act as modules which can be coherently coupled [36] to build larger processors and perform quantum error correction with minimal hardware overhead.

We thank Gerwin Koolstra for useful discussions and experimental assistance, and Shyam Shankar for a crit-

* These authors contributed equally to this work.
† David.Schuster@uchicago.edu

[1] A. Wallraff, D. I. Schuster, A. Blais, L. Frunzio, R.-S. Huang, J. Majer, S. Kumar, S. M. Girvin, and R. J. Schoelkopf, Nature **431**, 162 (2004).
[2] M. Reagor, W. Pfaff, C. Axline, R. W. Heeres, N. Ofek, K. Sliwa, E. Holland, C. Wang, J. Blumoff, K. Chou, et al., Physical Review B **94**, 014506 (2016).
[3] M. Reagor, H. Paik, G. Catelani, L. Sun, C. Axline, E. Holland, I. M. Pop, N. A. Masluk, T. Brecht, L. Frunzio, M. H. Devoret, L. Glazman, and R. J. Schoelkopf, App. Phys. Lett. **102**, 192604 (2013).
[4] R. W. Heeres, B. Vlastakis, E. Holland, S. Krastanov, V. V. Albert, L. Frunzio, L. Jiang, and R. J. Schoelkopf, Physical review letters **115**, 137002 (2015).
[5] R. W. Heeres, P. Reinhold, N. Ofek, L. Frunzio, L. Jiang, M. H. Devoret, and R. J. Schoelkopf, Nature communications **8**, 1 (2017).
[6] N. Ofek, A. Petrenko, R. Heeres, P. Reinhold, Z. Leghtas, B. Vlastakis, Y. Liu, L. Frunzio, S. Girvin, L. Jiang, M. Mirrahimi, M. J. Devoret, and R. J. Schoelkopf, Nature **536**, 441 (2016).
[7] L. Hu, Y. Ma, W. Cai, X. Mu, Y. Xu, W. Wang, Y. Wu, H. Wang, Y. Song, C.-L. Zou, S. M. Girvin, L.-M. Duan, and L. Sun, Nature Physics **15**, 503 (2019).
[8] P. Campagne-Ibarcq, A. Eickbusch, S. Touzard, E. Zalys-Geller, N. Frattini, V. Sivak, P. Reinhold, S. Puri, S. Shankar, R. Schoelkopf, et al., Nature **584**, 368 (2020).
[9] P. Reinhold, S. Rosenblum, W.-L. Ma, L. Frunzio, L. Jiang, and R. J. Schoelkopf, Nature Physics , 1 (2020).
[10] C. Wang, Y. Y. Gao, P. Reinhold, R. W. Heeres, N. Ofek, K. Chou, C. Axline, M. Reagor, J. Blumoff, K. Sliwa, et al., Science **352**, 1087 (2016).
[11] S. Rosenblum, Y. Y. Gao, P. Reinhold, C. Wang, C. J. Axline, L. Frunzio, S. M. Girvin, L. Jiang, M. Mirrahimi, M. H. Devoret, , and R. Schoelkopf, Nature communications **9**, 1 (2018).
[12] Y. Y. Gao, B. J. Lester, K. S. Chou, L. Frunzio, M. H. Devoret, L. Jiang, S. Girvin, and R. J. Schoelkopf, Na-

ture **566**, 509 (2019).

[13] F. Arute, K. Arya, R. Babbush, D. Bacon, J. C. Bardin, R. Barends, R. Biswas, S. Boixo, F. G. Brandao, D. A. Buell, *et al.*, Nature **574**, 505 (2019).

[14] P. Jurcevic, A. Javadi-Abhari, L. S. Bishop, I. Lauer, D. F. Bogorin, M. Brink, L. Capelluto, O. Günlük, T. Itoko, N. Kanazawa, *et al.*, Quantum Science and Technology **6**, 025020 (2021).

[15] N. M. Sundaresan, Y. Liu, D. Sadri, L. J. Szőcs, D. L. Underwood, M. Malekakhlagh, H. E. Türeci, and A. A. Houck, Physical Review X **5**, 021035 (2015).

[16] M. Mirhosseini, E. Kim, V. S. Ferreira, M. Kalaee, A. Sipahigil, A. J. Keller, and O. Painter, Nature communications **9**, 1 (2018).

[17] E. Kim, X. Zhang, V. S. Ferreira, J. Banker, J. K. Iverson, A. Sipahigil, M. Bello, A. Gonzalez-Tudela, M. Mirhosseini, and O. Painter, arXiv:2005.03802 (2020).

[18] S. Indrajeet, H. Wang, M. Hutchings, B. Taketani, F. K. Wilhelm, M. LaHaye, and B. Plourde, arXiv:2007.10932 (2020).

[19] J. P. Martinez, S. Léger, N. Gheeraert, R. Dassonneville, L. Planat, F. Foroughi, Y. Krupko, O. Buisson, C. Naud, W. Hasch-Guichard, *et al.*, npj Quantum Information **5**, 1 (2019).

[20] M. Pechal, P. Arrangoiz-Arriola, and A. H. Safavi-Naeini, Quantum Science and Technology **4**, 015006 (2018).

[21] J. Leppäkangas, J. Braumüller, M. Hauck, J.-M. Reiner, I. Schwenk, S. Zanker, L. Fritz, A. V. Ustinov, M. Weides, and M. Marthaler, Physical Review A **97**, 052321 (2018).

[22] R. Naik, N. Leung, S. Chakram, P. Groszkowski, Y. Lu, N. Earnest, D. McKay, J. Koch, and D. Schuster, Nature communications **8**, 1 (2017).

[23] See Supplemental Material [url] for a detailed description of the fabrication and characterization of flute cavities, the shielding and filtering used to improve transmon coherence and temperature, the schemes for universal control of the cavity modes, and the mode coherence measurements, which also includes Refs. [37–46].

[24] M. J. Reagor, *Superconducting Cavities for Circuit Quantum Electrodynamics*, Ph.D. thesis, Yale University (2016).

[25] A. V. Dixit, S. Chakram, K. He, A. Agrawal, R. K. Naik, D. I. Schuster, and A. Chou, arXiv:2008.12231 (2020).

[26] M. Kudra, J. Biznárová, A. Fadavi Roudsari, J. Burnett, D. Niepce, S. Gasparinetti, B. Wickman, and P. Delsing, Applied Physics Letters **117**, 070601 (2020).

[27] D. M. Pozar, *Microwave engineering* (John Wiley & Sons, 2009).

[28] L. Bretheau, P. Campagne-Ibarcq, E. Flurin, F. Mallet, and B. Huard, Science **348**, 776 (2015).

[29] S. Chakram, K. He, A. Dixit, A. Oriani, R. Naik, N. Leung, H. Kwon, W.-L. Ma, L. Jiang, and D. Schuster, arXiv:2010.15292 (2020).

[30] M. Pechal, L. Huthmacher, C. Eichler, S. Zeytinoğlu, A. A. Abdumalikov Jr, S. Berger, A. Wallraff, and S. Filipp, Physical Review X **4**, 041010 (2014).

[31] D. Schuster, A. Houck, J. Schreier, A. Wallraff, J. Gambetta, A. Blais, L. Frunzio, J. Majer, B. Johnson, M. Devoret, S. Girvin, and R. Schoelkopf, Nature **445**, 515 (2007).

[32] N. Khaneja, T. Reiss, C. Kehlet, T. Schulte-Herbrüggen, and S. J. Glaser, Journal of Magnetic Resonance **172**,

296 (2005).

[33] M. Hafezi, M. D. Lukin, and J. M. Taylor, New Journal of Physics **15**, 063001 (2013).

[34] B. M. Anderson, R. Ma, C. Owens, D. I. Schuster, and J. Simon, Physical Review X **6**, 041043 (2016).

[35] A. Romanenko, R. Pilipenko, S. Zorzetti, D. Frolov, M. Awida, S. Belomestnykh, S. Posen, and A. Grassellino, Physical Review Applied **13**, 034032 (2020).

[36] N. Leung, Y. Lu, S. Chakram, R. Naik, N. Earnest, R. Ma, K. Jacobs, A. Cleland, and D. Schuster, npj Quantum Information **5**, 1 (2019).

[37] S. B. Nam, Phys. Rev. **156**, 487 (1967).

[38] J. Zmuidzinas, Annual Review of Condensed Matter Physics **3**, 169 (2012).

[39] M. Tinkham, *Introduction to superconductivity* (Courier Corporation, 2004).

[40] H. Padamsee, *RF superconductivity: science, technology, and applications* (John Wiley & Sons, 2009).

[41] J.-H. Yeh, J. LeFebvre, S. Premaratne, F. C. Wellstood, and B. S. Palmer, Journal of Applied Physics **121**, 224501 (2017).

[42] Z. Wang, S. Shankar, Z. K. Minev, P. Campagne-Ibarcq, A. Narla, and M. H. Devoret, Phys. Rev. Applied **11**, 014031 (2019).

[43] K. Serniak, S. Diamond, M. Hays, V. Fatemi, S. Shankar, L. Frunzio, R. J. Schoelkopf, and M. H. Devoret, Phys. Rev. Applied **12**, 014052 (2019).

[44] S. E. Nigg, H. Paik, B. Vlastakis, G. Kirchmair, S. Shankar, L. Frunzio, M. H. Devoret, R. J. Schoelkopf, and S. M. Girvin, Physical Review Letters **108**, 240502 (2012).

[45] N. Leung, M. Abdelhafez, J. Koch, and D. Schuster, Physical Review A **95**, 042318 (2017).

[46] A. A. Clerk and D. W. Utami, Physical Review A **75**, 042302 (2007).